Band gaps and lattice solitons for the higher-order nonlinear Schrödinger equation with a periodic potential

Justin T. Cole and Ziad H. Musslimani
Department of Mathematics, Florida State University, Tallahassee, Florida 32306-4510, USA
(Received 21 February 2014; published 14 July 2014)

Localization and dynamics of the one-dimensional biharmonic nonlinear Schrödinger (NLS) equation in the presence of an external periodic potential is studied. The band-gap structure is determined using the Floquet-Bloch theory and the shape of its dispersion curves as a function of the fourth-order dispersion coupling constant β is discussed. Contrary to the classical NLS equation ($\beta = 0$) with an external periodic potential for which a gap in the spectrum opens for any nonzero potential, here it is found that for certain negative β, there exists a nonzero threshold value of potential strength below which there is no gap. For increasing values of potential amplitudes, the shape of the dispersion curves change drastically leading to the formation of localized nonlinear modes that have no counterpart in the classical NLS limit. A higher-order two-band tight-binding model is introduced that captures and intuitively explains most of the numerical results related to the spectral bands. Lattice solitons corresponding to spectral eigenvalues lying in the semi-infinite and first band gaps are constructed. In the anomalous dispersion case, i.e., $\beta < 0$ (where for the self-focusing nonlinearity no localized nonradiating solitons exist in the absence of an external potential), nonlinear finite-energy stationary modes with eigenvalues residing in the first band gap are found and their properties are discussed. The stability of various localized lattice modes is studied via linear stability analysis and direct numerical simulation.

DOI: 10.1103/PhysRevA.90.013815 PACS number(s): 42.65.Tg, 42.65.Jx, 05.45.Yv

I. INTRODUCTION

Linear and nonlinear optical wave propagation in nonhomogeneous media is a subject of great scientific importance with far-reaching technological applications [1,2]. The equation that governs such optical wave phenomena is a nonlinear Schrödinger-like equation in the presence of an external potential. In homogeneous media, linear waves typically tend to disperse or diffract whereas nonlinearity tends to either suppress or enhance this behavior, or leads to the formation of complex coherent structures.

The presence of inhomogeneities, on the other hand, can profoundly alter the wave dynamics and its linear and nonlinear behavior strongly depends on whether the medium it propagates in is periodic, quasiperiodic, or random. Generally speaking, for linear waves propagating in periodic media the spectrum is composed of an infinite union of closed intervals (called bands) separated by gaps. The field density (or intensity) exhibits a periodic pattern. The picture is quite different if the medium is random. In this case the spectrum is dense and the corresponding eigenfunctions are localized in space, a phenomenon known as Anderson localization. Finally, for waves propagating in quasicrystals (a state "in between" the periodic and random), the spectrum could exhibit a fractal structure with corresponding eigenfunctions that are localized in space.

In periodic structures, wave dynamics is typically governed by the interplay between dispersion and self-focusing (attractive) or self-defocusing (repulsive) nonlinearity. A delicate balance between these two effects results in the formation of a nonlinear coherent structure known in the literature as a lattice soliton [3]. These nonlinear lattice waves were first predicted in the discrete case (coupled waveguide arrays) by Christodoulides and Joseph [4] and later in photorefractive optical crystals [5–7]. Following these seminal papers, a large body of research work has emerged reporting on the existence and stability of various types of exotic lattice soliton structures in periodic, quasicrystals, and random media [8–23]. Moreover, discrete propagation and lattice spatial solitons have been also reported in nematic liquid crystals. In this regard, the nonlocality gives rise to novel, rich, and controllable phenomena such as all-optical Landau-Zener tunneling between diverse Floquet-Bloch bands, switching, and beam steering in tunable waveguide arrays [24–28].

Thus far, most of the studies on lattice solitons have concentrated on models combining external potentials (linear and/or nonlinear), Kerr-like and/or photorefractive nonlinearities, and a second-order diffraction or dispersion term with little attention (if any at all) on localization in periodic structures with higher-order dispersion or diffraction.

In this paper, we study wave propagation in a one-dimensional time-periodic lattice governed by the classical self-focusing and defocusing nonlinear Schrödinger (NLS) equation in the presence of a fourth-order dispersion

$$i\frac{\partial E}{\partial z} + \frac{1}{2}\frac{\partial^2 E}{\partial t^2} - \beta\frac{\partial^4 E}{\partial t^4} - V(t)E + g|E|^2E = 0\,, \qquad (1)$$

where, in the context of optics, the complex-valued function $E(t,z)$ corresponds to the slowly varying amplitude of the electric field, z is a scaled propagation distance, t is the temporal variable, β is a coupling constant taken to be either positive (normal dispersion) or negative (anomalous dispersion), and $g = \pm 1$. In Eq. (1), $V(t)$ represents a time crystal, which, optically, can be formed (as an example) by interfering two time-harmonic waves with different frequencies. The spectral properties of the corresponding linearized problem are identified and its band structure as a function of the coupling constant β is determined. We find that in the anomalous dispersion regime and for certain values of β a gap in the spectrum opens only for potential strengths exceeding a nonzero threshold value. This is contrary to the classical $\beta = 0$

case where a gap in the spectrum (for the linear problem) opens for any arbitrary strength of a periodic potential. Interestingly enough, we note that as the potential strength increases the geometric structure of the dispersion curves (i.e., curvature) changes its shape from being concave up to concave down. This is observed for both positive and negative values of β. Some of these numerical findings are explained analytically using a two-band discrete diatomic chain. Lattice solitons corresponding to eigenvalues in the semi-infinite and first gap are numerically constructed. Importantly, we have found stationary localized states in the anomalous dispersion case where in the absence of an external periodic potential (with $g = +1$) they fail to exist. The question of stability of various nonlinear modes is addressed.

The paper is organized as follows. In Sec. II we set up a general framework for the construction of band structure using Floquet-Bloch theory followed by a detailed numerical study of the geometric shape of the dispersion curves. In Sec. III we present a two-band discrete tight-binding model to intuitively explain our results found in previous sections. Nonlinear lattice modes with zero and multiple nodes are reported in Sec. IV and their stability properties (based on linear stability analysis as well as direct numerical simulations) are subsequently discussed in Sec. V. Finally, we conclude in Sec. VI.

II. FLOQUET-BLOCH THEORY AND SPECTRAL BAND GAP

We consider a lattice $V(t)$ with fundamental period T and denote by $\omega = 2\pi/T$ the period of its dual. To determine the properties of the band-gap structure, we linearize Eq. (1) around the trivial zero solution by writing $E(t,z) = \epsilon F(t)e^{-i\lambda z}$, $|\epsilon| \ll 1$ and obtain, to leading order in ϵ, the following spectral eigenvalue problem:

$$\mathbb{W}_\beta(\partial_t)F = \lambda F \ , \tag{2}$$

subject to the quasiperiodic boundary condition

$$F(t+T) = F(t)e^{i\mu T} \ , \tag{3}$$

where μ is the Floquet exponent and

$$\mathbb{W}_\beta(\partial_t) \equiv \beta\partial_t^4 - \partial_t^2/2 + V(t) \ . \tag{4}$$

Solutions to Eq. (2) satisfying Eq. (3) are constructed using Floquet-Bloch (FB) theory that enables one to decompose the eigenfunctions F in the product form

$$F(t,\mu) = G(t,\mu)e^{i\mu t} \ , \tag{5}$$

where $G(t)$ is a T periodic function. Equations (2) to (5) constitute a periodic boundary value problem for the eigenfunctions $G(t)$ and corresponding eigenvalues λ. When $\beta = 0$, it is known that the spectrum of $W_0(\partial_t)$ consists of an infinite union of closed intervals called spectral bands separated by gaps. As we will see later, the band-gap structure for the $\beta \neq 0$ case is highly nontrivial and its dispersion curves exhibit fundamentally different shape (hence supporting new types of lattice solitons) depending on whether the fourth-order dispersion term is normal or anomalous.

A. Normal dispersion regime

First, we consider problem (2) for $\beta > 0$ in the nearly lattice-free case for which the quantity $\varepsilon_V \equiv \max_{0\leqslant t\leqslant T}|V(t)|$ (a measure of the potential size) is very small compared to 1. In this limit, the band curves are approximately given (to leading order in ε_V) by

$$\lambda_n(\mu) = \Omega(\mu + \omega_n) \ , \tag{6}$$

where $\Omega(\xi) \equiv \xi^2/2 + \beta\xi^4$ and $\omega_n = n\omega$. This expression is valid for frequencies μ away from the Bragg points $P_{nm} \equiv -\omega(n+m)/2$ defined by $\lambda_n(P_{nm}) = \lambda_m(P_{nm})$ with integers $n \neq m$. Close to and at the Bragg points $s\omega/2$, for $s = \pm 1$, the correct form of the dispersion relation is obtained using a first-order degenerate perturbation theory

$$\lambda(\mu) \approx V_0 + \omega^2/8 + \beta\omega^4/16 \pm \left[V_1^2 + \gamma^2(\mu - s\omega/2)^2\right]^{1/2} \ , \tag{7}$$

valid for frequencies satisfying $|\mu - s\omega/2| \ll 1$ with $\gamma \equiv \omega(1+\beta\omega^2)/2$. A few remarks are now in order. (i) The measure of the gap at the edge of the first Brillouin zone (BZ), i.e., $\mu = s\omega/2$ is independent of β (at least to leading order in ε_V). (ii) Any small-enough periodic potential opens a gap in the spectrum similar to what happens for $\beta = 0$. The curvature of the dispersion bands (or the effective mass) near the edge of the BZ does change and it increases as β gets larger. As we shall see later, drastic changes take place for moderate and large values of potential amplitudes leading to a change in the curvature of the dispersion curves at the center (and edges) of the band.

To systematically explore the shape of the band-gap structure and verify the perturbation results, as well as to highlight its new features, we shall consider throughout the rest of the paper a periodic potential of the form

$$V(t) = U_0 \sin^2\left(\frac{\pi t}{2}\right), \quad U_0 \geqslant 0 \ . \tag{8}$$

We have numerically solved Eq. (2) subject to condition (3) using a Fourier collocation method outlined in Appendix A (this method is also known in the physics literature as partial wave expansion). For comparison, we have also used spectral and finite difference differentiation matrices [29,30]. Figures 1(a) and 1(b) show the first three band gaps for $\beta = 1/8$. The shaded regions (referred to as FB or spectral bands) represent eigenvalue and potential amplitude pairs (λ, U_0) that support bounded Bloch waves (5) with real μ, whereas the unshaded areas (band gaps) correspond to complex values of μ. The latter case can support localized lattice solitons that bifurcate from the edge or center of the BZ [31,32]. Moreover, the solid (dashed) lines trace the minimum (maximum) values of each single band. As one can see from Fig. 1(a), the global generic features of the dispersion curves in the *shallow lattice limit*, resembles that of the $\beta = 0$ case, i.e., the immediate opening of a gap. For comparison, we show in Fig. 1(c) the $\beta = 0$ case. However, we point out that for moderate lattice strengths a *significant* and *unexpected* behavior pertaining to the geometric characteristics of the dispersion bands occurs.

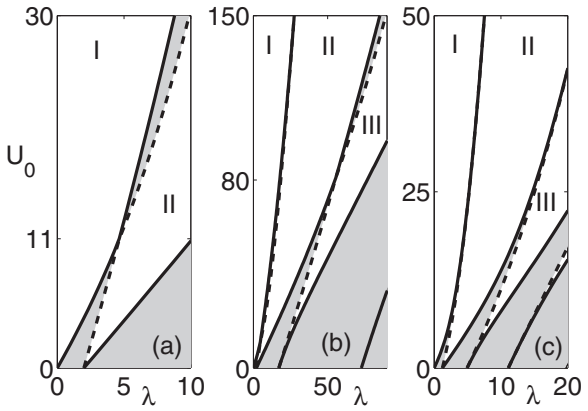

FIG. 1. Floquet-Bloch bands for (a, b) $\beta = 1/8$, (c) $\beta = 0$ as a function of U_0. Regions I, II, and III are the semi-infinite, first, and second band gaps, respectively. The solid (dashed) line shows $\min \lambda(\mu)[\max \lambda(\mu)]$.

The local curvature of the first band at the center (edges) of the first BZ changes its sign from positive (negative) at $U_0 = 5$ to negative (positive) at $U_0 = 25$ (see Fig. 2). The critical value $U_0^{\rm cr}$ needed to flip the local concavity of the first band depends, of course, on the fourth-order dispersion term: the larger β is, the higher $U_0^{\rm cr}$ becomes. Similar observations have been reported in [33] for the zigzag discrete model where a change in the curvature of the dispersion band occurs *only* at the edges of the BZ. This local behavior equally extends to higher-order bands. For example, at $U_0 \approx 80$ the second band does change its curvature at the center of the BZ, but this time from negative to positive. It is worth noting that the sign of the curvature at the first and second FB band minima and maxima points does not change (see first and third rows in Fig. 2).

Generally speaking, the symmetry and periodicity of the Floquet-Bloch modes determine the kind of lattice solitons that will bifurcate from the band edges. With this in mind, we show in Fig. 3 typical real-valued FB modes with periods 2 and 4 corresponding to $\mu = 0$ and $\mu = \pm\pi/2$, respectively. When approaching the first dispersion curve from the semi-infinite (first) gap the band-edge location (in μ) depends on U_0. Indeed, in the shallow lattice limit, this happens at $\mu = 0(\pm\pi/2)$ and the FB mode has period 2(4) as shown in Fig. 3(a) [Fig. 3(b)].

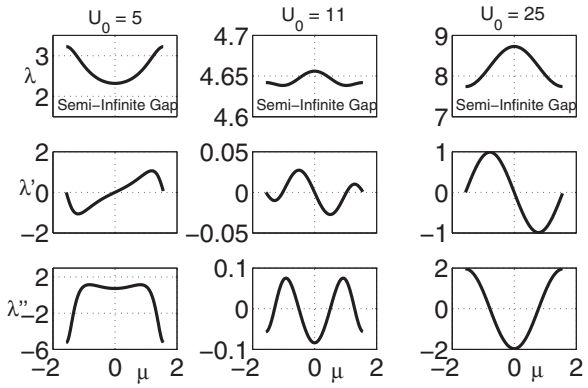

FIG. 2. From top to bottom: First FB band, group velocity, and curvature for $\beta = 1/8$ at various values of U_0.

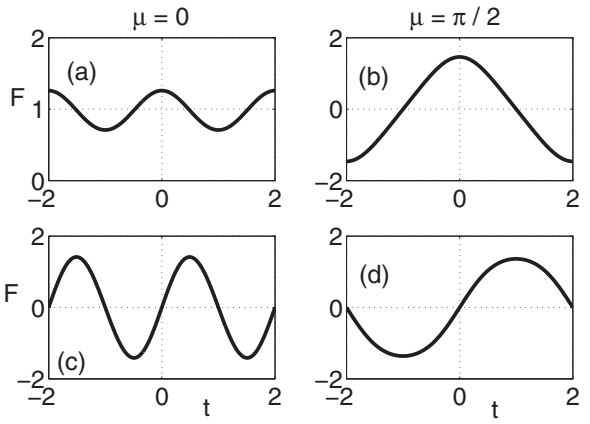

FIG. 3. FB modes (unnormalized) for $\beta = 1/8$ and $U_0 = 5$. The first (second) row corresponds to the first (second) band.

However, this is not the case in the deep lattice limit, where for the same β the band edge encountered from the semi-infinite (first) gap is now located at $\mu = \pm\pi/2(0)$ and the new corresponding FB mode now has period 4(2). Similar arguments related to the periodicity of the FB modes as well as the flipping of the edges equally hold for the second band [Figs. 3(c) and 3(d)]. As we shall see in Sec. IV, this switching of the Bloch modes will result in the formation of new types of lattice solitary waves bifurcating from the newly formed band edge.

B. Anomalous dispersion regime

In this section we study the band structure for the negative β case. We have identified two major peculiarities that have no counterpart whatsoever in the $\beta \geqslant 0$ regime. First, in the shallow lattice limit we have numerically found a nonzero threshold value $U_0^{\rm th}$ dependent on β, below which there is no gap in the spectrum. This is in sharp contrast to the $\beta = 0$ case for which a gap exists for any nonzero periodic potential. Such behavior is clearly illustrated in Fig. 4. Our numerical experiments seem to indicate that the threshold required to

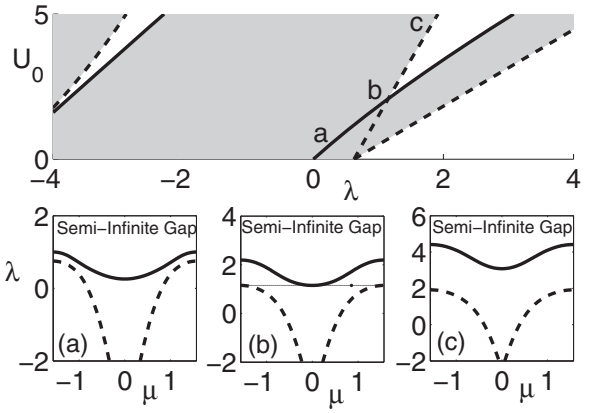

FIG. 4. (Top) Band structure for $\beta = -1/10$ where shaded regions indicate spectral bands. The solid (dashed) line gives $\min \lambda(\mu)(\max \lambda)$. Figs. (a),(b) and (c) depicts the first (solid line) and second (dashed line) bands at $U_0 = 0.5, 2.0835, 5$, respectively.

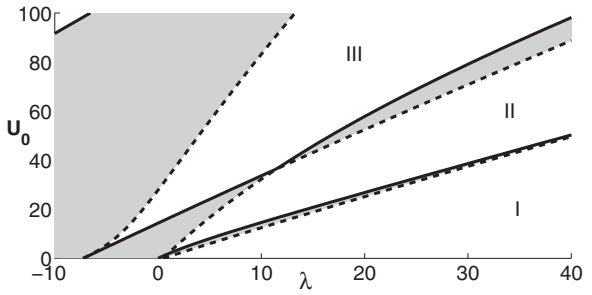

FIG. 5. Band-gap structure for $\beta = -1/8$ and various values of U_0. Regions I, II, and III correspond to the semi-infinite, first, and second band gaps, respectively. The solid and dashed lines indicate minimum and maximum values of λ.

open a gap exists only for $|\beta| \lesssim 2/\pi^2$ and changes as $|\beta|$ gets smaller.

To support our numerical findings, we resort to perturbation theory assuming a shallow lattice limit and coupling constant β satisfying $|\beta|\omega^2 > 1$. In this case, the curves λ_0 and λ_{-1} intersect at the point $\mu = \omega/2$. Inspecting Eq. (7) at that point shows that there exists $\beta_*(\omega) > 0$ for which $\omega^2/8 - |\beta|\omega^4/16 > \lambda_0(0)$ for any $|\beta| < \beta_*(\omega)$ (recall that V_0 and V_1 are arbitrarily small), hence no global gap exists. We would like to point out that the lack of a global gap for small potentials is reminiscent of the two-dimensional linear Schrödinger equation $[\partial_x^2 + \partial_y^2 + \mathcal{V}(x,y)]\Psi = E\Psi$ with periodic $\mathcal{V}$ where a gap in the spectrum exists only if $\max(\mathcal{V}) > \mathcal{V}_{\text{th}}$. So in essence, there is a "trade-off" between dimensionality and higher-order dispersion. The full range of eigenvalues versus potential amplitudes is shown in Fig. 5 for $\beta = -1/8$. The second interesting property we have observed is the flattening-out and local concavity change of the second band at moderate values followed by a change in the first band at higher U_0. Note that this is the opposite of what happened in the $\beta > 0$ case. In particular, Fig. 6 shows a zoom-in of the band dynamics at the center of the BZ. The second dispersion band evolves from a V-shaped curve at moderate potential values to a single hump-like form at higher strengths.

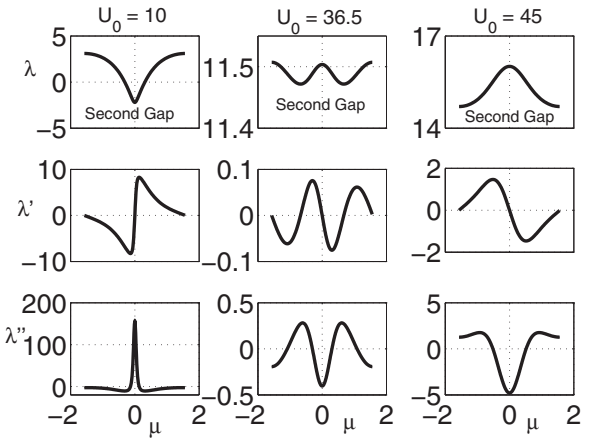

FIG. 6. From top to bottom: The second FB bands, group velocity, and group velocity dispersion for $\beta = -1/8$ and various values of U_0.

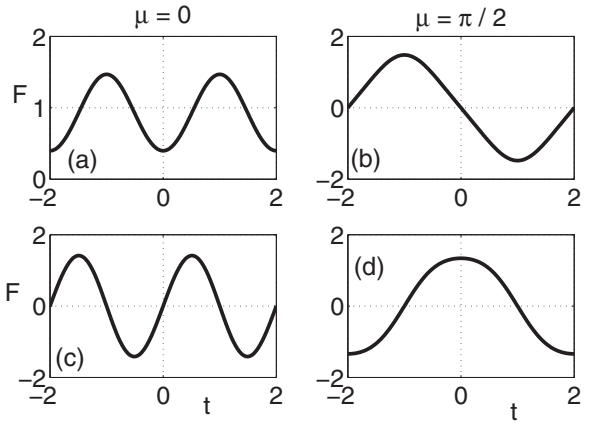

FIG. 7. FB modes (unnormalized) for $\beta = -1/8$ and $U_0 = 10$. The first (second) row corresponds to the first (second) band.

While the band curves for the anomalous case change drastically in comparison with $\beta > 0$, the FB modes, on the other hand, seem to largely preserve their symmetry properties and periodicity at the center of the BZ with a slight difference in parity at the edge of the BZ (see Fig. 7 right column).

III. TIGHT-BINDING LIMIT: HIGHER-ORDER DIATOMIC CHAIN

In the preceding sections, some of the intriguing structure of the dispersion band curves were obtained in the moderate to deep lattice regime. It is in that limit where part of the previous results can be intuitively understood and explained using a simplified linear discrete two-band tight-binding model. The configuration we have in mind is shown in Fig. 8. The basic unit cell is composed of two types of "atoms" periodically extended along a lattice of integer index n. The nth position of both atoms is labeled a_n and b_n, respectively. We assume that the coupling constants between nearest neighbor $\{(a_n,b_n),(b_{n-1},a_n)\}$ and next-nearest neighbor $\{(a_n,a_{n+1}),(b_n,b_{n+1})\}$ for $n \in \mathbb{Z}$ are given by $1,c > 0,\kappa_1,\kappa_2$, respectively.

The equations describing wave propagation in such a linearly coupled diatomic chain are given by

$$i\frac{da_n}{dz} + b_n + cb_{n-1} + \kappa_1(a_{n+1} + a_{n-1}) = 0\,, \tag{9}$$

$$i\frac{db_n}{dz} + ca_{n+1} + a_n + \kappa_2(b_{n+1} + b_{n-1}) = 0\,. \tag{10}$$

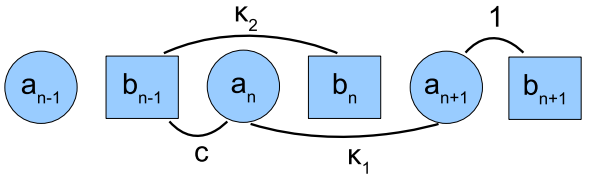

FIG. 8. (Color online) Schematic illustration of the diatomic lattice model. Shown are the coupling constants between different sites.

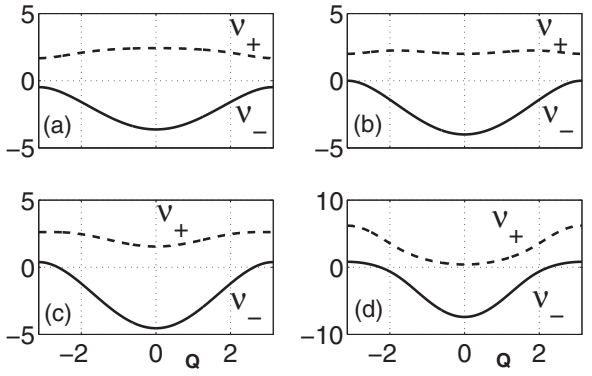

FIG. 9. Dispersion relation (13) for $c = 2, \kappa_1 = 1/2$, and $\kappa_2 =$ (a) 1/10, (b) 1/2, (c) 1, and (d) 3.

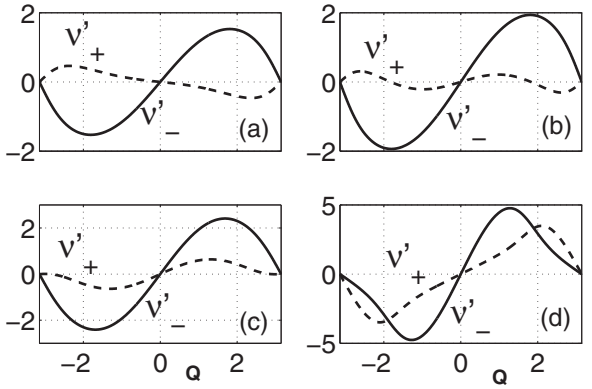

FIG. 10. Group velocity (20) for $c = 2, \kappa_1 = 1/2$ and $\kappa_2 =$ (a) 1/10, (b) 1/2, (c) 1, and (d) 3.

We then assume a plane-wave solution, the so-called discrete Floquet-Bloch mode, of the form

$$a_n(z) = Ae^{iQn}e^{-i\nu z}\,, \tag{11}$$

$$b_n(z) = Be^{iQn}e^{-i\nu z}\,, \tag{12}$$

where A, B are constant amplitudes, ν is the longitudinal wave number (spatial eigenenergy), and Q is the real Bloch momentum that lies within the reduced BZ $[-\pi,\pi]$. Substituting Eqs. (11) and (12) into Eqs. (9) and (10) we find a nontrivial solution to exist only if the wave number ν satisfies

$$\nu_\pm(Q) = -(\kappa_1+\kappa_2)\cos(Q) \pm \Lambda^{1/2}(Q)\,, \tag{13}$$

$$\Lambda(Q) = (\kappa_1-\kappa_2)^2\cos^2(Q) + 2c\cos(Q) + c^2 + 1\,. \tag{14}$$

Notice that $\nu_\pm$ admits the symmetries

$$\nu_\pm(-\kappa_1,-\kappa_2) = -\nu_\mp(\kappa_1,\kappa_2)\,, \tag{15}$$

$$\nu_\pm(\kappa_1,\kappa_2) = \nu_\pm(\kappa_2,\kappa_1)\,. \tag{16}$$

Throughout the rest of the paper, we fix the model parameters to, for example, $c = 2$ and $\kappa_1 = 1/2$ and consider only positive values of κ_2. Our results can be extended to the negative $\kappa_j, j = 1,2$ case by using the symmetry relation (15). The dispersion relation $\nu_\pm$ is shown in Fig. 9 for various values of κ_2. It is obvious that there is a profound change in the local geometric structure of the ν_+ branch shape (i.e., the flipping of curvature), whereas the graph of the lower part (ν_-) is almost unaffected. We remark that if $\kappa_1 = -1/2$ and κ_2 is negative, then the sign of the curvature of the lower band changes as $|\kappa_2|$ increases, leaving the upper band unaffected. Similar qualitative behavior was observed in Secs. II A and II B where a "reorientation" of the first and second bands took place at moderate-to-large potential amplitudes (near the tight-binding limit). To shed more light on the local behavior of the dispersion relation we examine its long wave limit when $Q \to 0$. In this case, Eq. (13) yields

$$\nu_\pm \approx a_0^\pm + a_2^\pm Q^2/2\,, \tag{17}$$

where

$$a_0^\pm = -(\kappa_1+\kappa_2) \pm [(\kappa_1-\kappa_2)^2 + (1+c)^2]^{1/2}\,, \tag{18}$$

$$a_2^\pm = \kappa_1+\kappa_2 \mp \frac{c+(\kappa_1-\kappa_2)^2}{[(\kappa_1-\kappa_2)^2+(1+c)^2]^{1/2}}\,. \tag{19}$$

Scrutinizing the expression for a_2^- shows that the lower dispersion branch ν_- always resembles an up-facing parabola with a positive-definite curvature whereas the upper one (ν_+) changes its local curvature from negative to positive at some $\kappa_2 = \kappa_2^*(c,\kappa_1)$. Further increasing the value of κ_2 results in disappearance of the gap and it remains closed for all larger values of κ_2 [see Fig. 9(d)]. This is, of course, unrealistic since this happens when the next-nearest neighbor coupling κ_2 is more dominant than the nearest-neighbor ones.

The group velocity and group velocity dispersion are readily obtained from Eq. (13) and are given, respectively, by

$$\frac{d\nu_\pm}{dQ} = \sin(Q)(\kappa_1+\kappa_2) \pm \frac{1}{2}\Lambda^{-1/2}\Lambda_Q\,, \tag{20}$$

$$\frac{d^2\nu_\pm}{dQ^2} = \cos(Q)(\kappa_1+\kappa_2) \pm \frac{1}{2}\Lambda^{-1/2}\left(\Lambda_{QQ} - \frac{1}{2}\Lambda^{-1}\Lambda_Q^2\right), \tag{21}$$

$$\Lambda_Q = -\sin(2Q)(\kappa_1-\kappa_2)^2 - 2c\sin(Q), \tag{22}$$

$$\Lambda_{QQ} = -2\cos(2Q)(\kappa_1-\kappa_2)^2 - 2c\cos(Q). \tag{23}$$

As is expected, the curvature of the lower branch ν_- remains positive at the center of the BZ and negative at the edges. On the other hand, at $Q = 0(\pm\pi)$ the upper branch's group velocity dispersion changes its sign from negative (positive) to positive (negative). These discrete group velocity and curvature shown in Figs. 10 and 11, respectively, qualitatively agree with the continuous cases discussed in Figs. 2 and 6.

It can be seen in Fig. 11 that the slope of the lower branch group velocity dispersion is positive for $-\pi < Q < 0$ and negative for $\pi > Q > 0$. The upper branch clearly changes its group velocity dispersion from negative to positive at the center of the BZ.

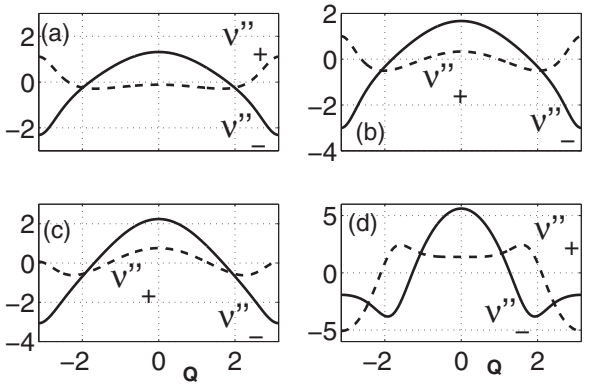

FIG. 11. Group velocity dispersion (21) for $c = 2, \kappa_1 = 1/2$, and $\kappa_2 =$ (a) 1/10, (b) 1/2, (c) 1, and (d) 3.

IV. LATTICE SOLITONS

In this section we find gap soliton solutions to Eq. (1) for the nonlinearity coefficient $g = \pm 1$ and eigenvalues residing in either the semi-infinite or first band gaps identified in Secs. II A and II B. Families of both positive and negative β solutions corresponding to moderate potential amplitudes $0 < U_0 \lesssim 10$ as well as large amplitudes $U_0 \gtrsim 25$ are numerically constructed using the fixed-point spectral renormalization scheme outlined in Appendix B. Recall that in the absence of an external potential it is known [34,35] that in the *anomalous dispersion regime* ($\beta < 0$) *with* $g = +1$ *localized nonradiating solutions to* Eq. (1) *do not exist*. Here, we show that the presence of a periodic potential can "trap" the radiation and lead to self-induced localized nonradiating stationary modes with negative β. The corresponding soliton eigenvalue depends on the sign of g. For $g = +1$ they lie in the first gap, whereas for $g = -1$ they reside either in the semi-infinite or first gap. One interesting aspect of our lattice solitons is that certain family members bifurcate from band edges that have no counterpart whatsoever in the classical limit ($\beta = 0$). Similar to the classical NLS limit [36], the present band-gap solutions happen to bifurcate from band edges where $\mathrm{sgn}(\lambda'')$ is the same as g. In addition, we find two bifurcating families of soliton solutions: one on-site (centered around a lattice minimum) and the other off-site (centered around a lattice peak). For the classical case, all ground-state solutions are on-site [36]. We remark that lattice solitons also exist in nematic liquid crystals in which their structure and dynamics exhibit rich behavior due to the presence of nonlocality [24–28].

A. Normal dispersion regime

1. Shallow-to-moderate potentials

In Fig. 12 we show typical lattice solitons for $\beta = 1/8$ and potential amplitude $U_0 = 5$ corresponding to various eigenvalues residing in the semi-infinite and first band gap. The solutions shown in Figs. 12(b), 12(d), and 12(e) bifurcate from the corresponding band edge inheriting the symmetries, parity, and fine structure of the Bloch functions depicted in Figs. 3(a), 3(d), and 3(b), respectively. These localized solutions are all on-site (even or odd about $t = 0$). We have already seen in Sec. II A for the shallow lattice limit and in the

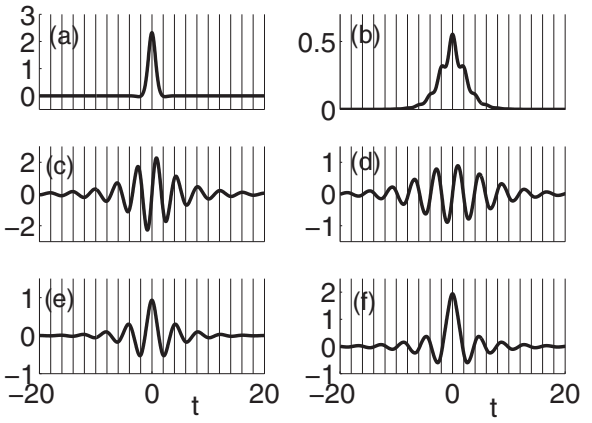

FIG. 12. Lattice solitons for $\beta = 1/8$ and $U_0 = 5$ (see Fig. 13 for the location of the corresponding eigenvalues in the power curve). In panels (a), (b), (c), and (d), $g = +1$ at eigenvalues $\lambda = -1, 2.2, 3.3, 5.4$, respectively. Panels (e) and (f) correspond to $g = -1$ and eigenvalues $\lambda = 3.5, 5.6$, respectively. Vertical lines indicate potential minima.

normal dispersion regime that the linear dispersion bands and Floquet-Bloch modes largely resemble the $\beta = 0$ case. Thus it is no surprise that all the modes shown in Fig. 12 look similar to those found in [32,36]. Near the bifurcating band edges the solutions are low-amplitude and broad (occupying many lattice sites). Far from the bifurcating band edge the lattice solitons are highly localized (occupying few lattice sites). The power curves versus soliton eigenvalue is shown in Fig. 13 for $g = \pm 1$. These curves trace a continuous one-parameter (i.e., λ) family of solutions for different g and band gaps. Lattice solitons in the same family typically inherit characteristic properties of the Bloch wave parent they bifurcate from, e.g., symmetry, parity, and fine-structure periodicity. The right solid line traces the first gap soliton family bifurcating from the left edge of the second band, whereas the dashed line follows a different family of modes bifurcating from the first band. Finally, the left solid curve shown in Fig. 13 traces a new family of solutions bifurcating from the left side of the first band into the semi-infinite gap.

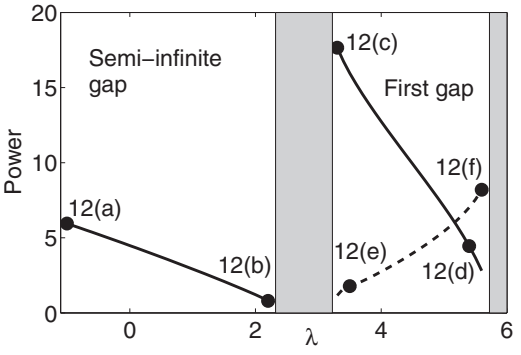

FIG. 13. Power curves for $\beta = 1/8$ and $U_0 = 5$. Each point on the solid ($g = +1$) and dashed ($g = -1$) lines represents a soliton solution. Typical profiles of such solutions are shown in Fig. 12.

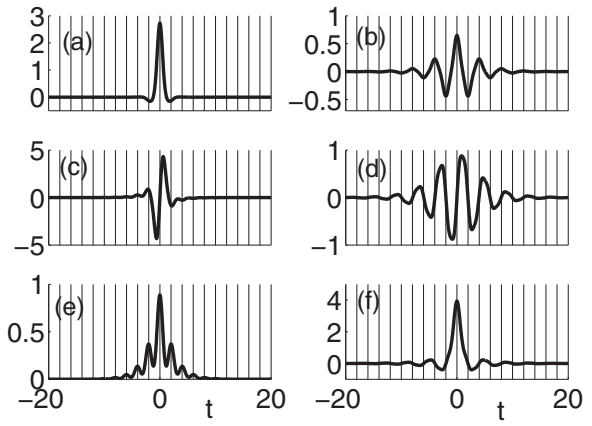

FIG. 14. Lattice solitons for $\beta = 1/8$ and $U_0 = 25$ (see Fig. 15 for the location of the corresponding eigenvalues in the power curve). In panels (a), (b), (c), and (d), $g = +1$ at eigenvalues $\lambda = 3, 7.6, 9.1, 19.8$, respectively. Panels (e) and (f) correspond to $g = -1$ and eigenvalues $\lambda = 9, 19.9$, respectively. Vertical lines indicate potential minima.

2. *Large potentials*

Next we consider families of lattice solitons in the large potential regime ($U_0 = 25$). Recall from Sec. II A that in this limit the first band changed its geometric characteristics. As a result, the solitons will bifurcate from the edge (rather than the center) of the BZ when approached from the semi-infinite gap. Alternatively, at the first band the lattice modes will now bifurcate from the center of the BZ (rather than the edges) if approached from the first gap. This unusual behavior of the band structure will evidently have to affect the bifurcating soliton family. Indeed Fig. 14 shows new solutions with no counterpart whatsoever in the $\beta = 0$ case. For example, the soliton in Fig. 14(b) is fundamentally different than that of Fig. 12(b), in spite of the fact they both bifurcate into the semi-infinite gap. The latter is positive-definite and has a two-periodic fine structure, whereas the former is sign-indefinite and four-periodic [and vice versa for the solutions in Figs. 14(e) and 12(e)]. A further consequence of the first band-gap reorientation is that the first gap family of solutions does not preserve their fast scale periodicity in moving from one band edge to the other. For instance, the bifurcating solution Fig. 14(d) has four-periodic fine structure while the soliton in Fig. 14(c) (belonging to the same family) is two-periodic near the opposite band edge where the corresponding FB mode has the same period. The lattice soliton existence curves (also called power curves) corresponding to Fig. 14 are shown in Fig. 15.

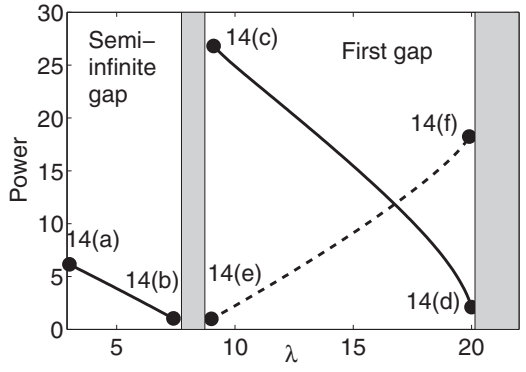

FIG. 15. Power curves for $\beta = 1/8$ and $U_0 = 25$. Each point on the solid ($g = +1$) and dashed ($g = -1$) lines represents a soliton solution. Typical profiles of such solutions are shown in Fig. 14.

B. Anomalous dispersion regime

1. *Shallow-to-moderate potentials*

In the preceding section, we have seen that most of the interesting features of the lattice solitons came from the unusual geometric structure of the dispersion bands (primarily the locations of the band edges). While most of the intriguing behavior of the nonlinear modes will naturally extend to the anomalous dispersion regime, one important difference is that here we find localized nonradiating solutions (for $g = +1$) that cease to exist when $U_0 = 0$. Figure 16 shows such and other solutions for eigenvalues residing in the semi-infinite and first gap where $\beta = -1/8$ and $U_0 = 10$. The solutions depicted in Figs. 16(a), 16(c), and 16(f) bifurcate from the corresponding Bloch modes shown in Figs. 7(b), 7(d), and 7(a), respectively. These solutions bear little resemblance to those found when $\beta > 0$. The most striking feature we have observed is the off-site (around $t = 1$) structure of certain solution sets [see Figs. 16(a), 16(b), 16(e), and 16(f)]. Recall that in the previous section ($\beta > 0$) and earlier work [32,36] ($\beta = 0$) all the ground-state solutions found are on-site. It appears that these solitons acquire the fine structure (periodicity) of the corresponding Bloch waves, but take different Bloch symmetries. For instance, the Bloch mode in Fig. 7(b) is indeed odd around $t = 0$, however, it is also even about $t = 1$. The lattice solitons shown in Figs. 16(a), 16(b), 16(e), and 16(f) take even symmetries around the lattice maximum $t = 1$, whereas Figs. 16(c) and 16(d) have even symmetry centered at $t = 0$. Similar to the first gap soliton family ($\beta > 0$), the bifurcating solution in Fig. 16(c) has a four-periodic fast scale

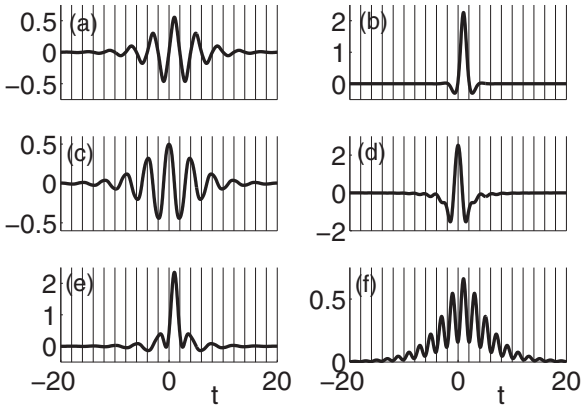

FIG. 16. Lattice solitons for $\beta = -1/8$ and $U_0 = 10$ (see Fig. 17 for the location of the corresponding eigenvalues in the power curve). In panels (a), (b), (c), and (d), $g = -1$ at eigenvalues $\lambda = 8.2, 11, 3.2, 6.1$, respectively. Panels (e) and (f) correspond to $g = +1$ and eigenvalues $\lambda = 3.2, 6.3$, respectively. Vertical lines indicate potential minima.

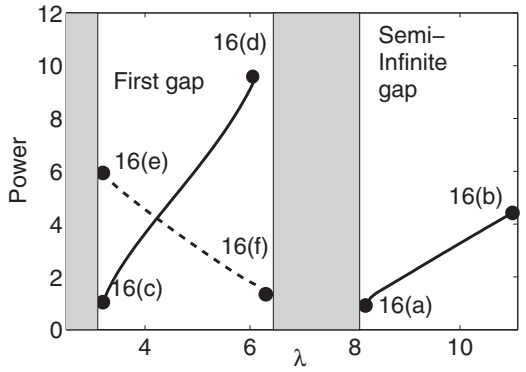

FIG. 17. Power curves for $\beta = -1/8$ and $U_0 = 10$. Each point on the solid ($g = -1$) and dashed ($g = +1$) lines represents a soliton solution. Typical profiles of such solutions are shown in Fig. 16.

while the solution in Fig. 16(d) is in the same family, yet has period 2. The soliton existence curve is shown in Fig. 17 for eigenvalues lying inside the semi-infinite and first band gaps. It should be noted that these solutions bifurcate from band edges whose curvature sign equals that of g. The family of solutions with $g = -1$ (corresponding to the left solid line in Fig. 17) bifurcate from the right side of the second band and the solutions with $g = +1$ (shown by the dashed line in Fig. 17) bifurcate from the left edge of the first band. Finally, note for $g = -1$ a solution family is traced in the semi-infinite gap (as shown by the right solid line in Fig. 17) from the right edge of the first band.

2. *Large potentials*

Finally, we discuss here the formation of coherent structures in the deep lattice limit ($U_0 = 45$). In Sec. II B, we saw that in this regime the second band changed its local curvatures at the center and edges of the BZ. Thus, we expect all lattice solitons with corresponding eigenvalues near the second band edge to admit alternative features, similar to what occurred in the normal dispersion case. We again emphasize that most of our findings share no similarities with either the classical NLS limit or the positive β case. Indeed, Fig. 18 depicts representatives from each family. The solution shown in Fig. 18(c) now bifurcates from the second band at the center of the BZ (rather than the edge) and consequently is now off-site (centered around $t = 1$) with odd parity and a two-periodic fine structure. We also see the solution in Fig. 18(e) has fine period 2 as opposed to the four-periodic solution in Fig. 16(e). We remark that many of the lattice soliton characteristics can be understood from the power curves shown in Fig. 19.

V. STABILITY ANALYSIS

Having found a large families of lattice soliton solutions we turn our attention in this section to the question of stability. We carry out a numerical linear stability analysis and supplement it with direct numerical simulations. To determine the linear stability properties of a lattice soliton family member ($\beta \neq 0$) we consider small perturbations on solutions to Eq. (1) of the

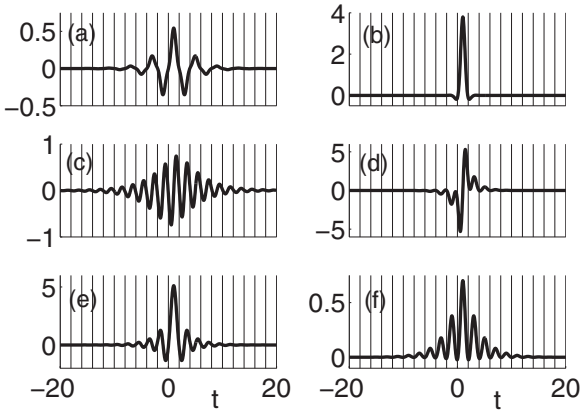

FIG. 18. Lattice solitons for $\beta = -1/8$ and $U_0 = 45$ (see Fig. 19 for the location of the corresponding eigenvalues in the power curve). In panels (a), (b), (c), and (d), $g = -1$ at eigenvalues $\lambda = 36.3, 46, 16.2, 34.8$, respectively. Panels (e) and (f) correspond to $g = +1$ and eigenvalues $\lambda = 16.5, 35.3$, respectively. Vertical lines indicate potential minima.

form

$$E(t,z) = [\phi(t) + \chi(t,z)]e^{-i\lambda z}\,, \tag{24}$$

where the "size" of $|\chi|$ is much smaller than that of ϕ. Linearizing around the solution $\phi(t)$ we find, to leading order in χ, the stability equation

$$i\frac{\partial \chi}{\partial z} + \lambda\chi + \frac{1}{2}\frac{\partial^2 \chi}{\partial t^2} - \beta\frac{\partial^4 \chi}{\partial t^4} - V(t)\chi + g\phi^2\chi^* + 2g|\phi|^2\chi = 0\,. \tag{25}$$

This evolution equation governs the perturbation $\chi(t,z)$ subject to a localized initial condition $\chi(t,0)$ and boundary conditions $\chi \to 0$ as $|t| \to \infty$.

Let us for now assume that the evolution of this perturbation is exponential in z, i.e.,

$$\chi(t,z) = [v(t) + w(t)]e^{\sigma z} + [v^*(t) - w^*(t)]e^{\sigma^* z}\,. \tag{26}$$

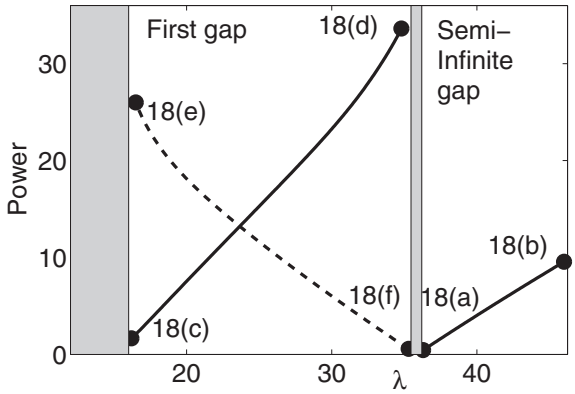

FIG. 19. Power curves for $\beta = -1/8$ and $U_0 = 45$. Each point on the solid ($g = -1$) and dashed ($g = +1$) lines represents a soliton solution. Typical profiles of such solutions are shown in Fig. 18.

Substituting Eq. (26) into Eq. (25) results in the following eigenvalue problem:

$$i\mathcal{M}\mathcal{Y} = \sigma\mathcal{Y}\,, \tag{27}$$

which can be solved for the eigenvalue σ and its corresponding eigenfunction $\mathcal{Y} \equiv (v,w)^T$. Here, we define

$$\mathcal{M} = \begin{pmatrix} \mathbb{M}_1 & -\mathbb{W}_\beta + \mathbb{M}_2 \\ -\mathbb{W}_\beta + \mathbb{M}_3 & -\mathbb{M}_1 \end{pmatrix},$$

$$\mathbb{M}_1 = \frac{g}{2}[\phi^2 - (\phi^*)^2],$$

$$\mathbb{M}_2 = \lambda + 2g|\phi|^2 - \frac{g}{2}[\phi^2 + (\phi^*)^2],$$

$$\mathbb{M}_3 = \lambda + 2g|\phi|^2 + \frac{g}{2}[\phi^2 + (\phi^*)^2]. \tag{28}$$

The nonlinear mode $\phi(t)$ is said to be exponentially unstable if σ has a nonzero real component, neutrally stable if σ is purely imaginary, and oscillatory unstable if $\sigma \in \mathbb{C}$. Since all the eigenmodes $\phi(t)$ we found in the previous section are real-valued, by symmetry arguments, if σ is an eigenvalue of Eq. (27) with eigenfunction $\mathcal{Y}$, so is $-\sigma^*$ with corresponding eigenfunction $\mathcal{Y}^*$.

The standard direct approaches to numerically solving Eq. (27) are to truncate the domain on some large grid and represent the derivatives by differentiation matrices [29,30] or instead to represent the functions in terms of their respective Fourier series [37]. However, it is known in the literature [38,39] that the discretization of continuous eigenvalue problems (particularly nonsymmetric) can lead to the generation of spurious eigenvalues. Alternative approaches include iterative schemes [40] as well as the Evans function method [36,41–43]. Theoretical approaches to characterize the spectral properties of Eq. (27) ($\beta = 0$) have been intensively studied [44–46]. Here we address the question of stability in three different manners: (i) integrate Eq. (25) using a random localized initial condition; (ii) solve Eq. (27) via standard discretization methods; and (iii) monitor the nonlinear evolution of an initially perturbed solution to Eq. (1) through direct numerical simulation (DNS). All the results presented below concerning the computation of the unstable eigenvalues σ are based on the Fourier collocation method and found to agree well with the spectral or finite-difference differentiation matrices used to approximate all derivatives. We use explicit fourth-order schemes to integrate in z, either by a spectral Runge-Kutta or split-step Fourier method.

A. Normal dispersion case

To begin with, we remark that all sufficiently low-intensity solutions with eigenvalues λ close enough to any bifurcating band edge (regardless of the values for β, g, and U_0) are exponentially stable, in the sense of Eq. (26). Intuitively speaking, these are broad, low-amplitude solutions nearly corresponding to linear-bounded Bloch waves. Consequently, the nonlinear terms appearing in Eq. (27) can be neglected so that λ is nearly in the spectrum of $\mathbb{W}_\beta$, implying $\sigma \approx 0$. With this in mind, we shall consider only cases where the soliton eigenvalues are away from any bifurcating band edge. Also, we present stability results only for a representative of each soliton family rather than scanning individual cases.

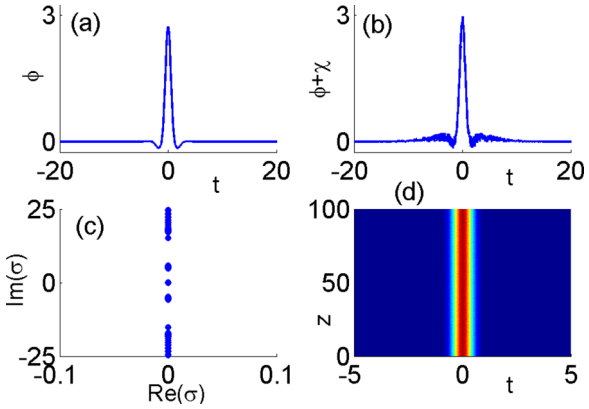

FIG. 20. (Color online) (a) Lattice soliton $\phi(t)$ given in Fig. 14(a) with $\max|\phi| \approx 2.73$. (b) $\phi(t) + \chi(t,0)$ where $\chi(t,0)$ is the perturbation given in Eq. (29) for one realization of randomness and $\varepsilon = 0.1$. (c) Spectrum of the linear stability eigenvalue problem (27) corresponding to the lattice soliton in panel (a). (d) Dynamic stability obtained by direct numerical simulation using Eq. (1) with initial condition shown in panel (b).

Now, consider the family of solutions corresponding to $\beta = 1/8$ shown in Figs. 12 and 14. First, we present stability results concerning the semi-infinite gap solution depicted in Fig. 14(a). We have also obtained stability results (not shown here) for the soliton shown in Fig. 12(a) and found similar conclusions to the former case. The spectrum of the eigenvalue problem (27) is shown in Fig. 20(c). It is located entirely on the imaginary axis (thus the lattice mode is exponentially or neutrally stable) and the corresponding eigenfunctions are bounded and oscillatory. To extend the stability analysis beyond the linear regime we resort to direct numerical simulations. To this end, we initially seed the soliton with a random and localized perturbation in the form

$$\chi(t,0) = \varepsilon \max_\tau |\phi(\tau)|\delta_r(t)e^{-t^2/50}\,, \tag{29}$$

and monitor its evolution using Eq. (1). Here, ε is a small positive parameter and $\delta_r(t)$ is a random function of t chosen as follows. Upon discretizing t, i.e., $t \to t_j$, the function $\delta_r(t)$ is replaced by $\delta_r(t_j)$, which is defined at the grid points t_j by a random number uniformly distributed in $[0,1]$. All results were performed for one realization of the random function $\delta_r(t)$. A typical perturbed semi-infinite gap solution along with its stable nonlinear evolution are shown in Fig. 20. The random perturbation seems to be completely washed out and the input beam persists for a relatively long distance. Our results are consistent with the $\beta = 0$ case where on-site lattice solutions were also found to be linearly and nonlinearly stable [32,36]. Thus, one could conclude that the addition of a normal fourth-order dispersion does not seem to cause any drastic deviation regarding the stability properties of these lattice solitons.

When numerically solving eigenvalue problem (27) for lattice solitons corresponding to eigenvalues in the first band gap, spurious eigenvalues seem to emerge. Therefore, we adopt instead the dynamics approach to linear stability and simulate Eq. (25) subject to initial condition (29). Moreover, we shall use the quantity $\max_t |\chi(t,z)|$ as a guiding measure for the development of any instability or the lack thereof. In particular,

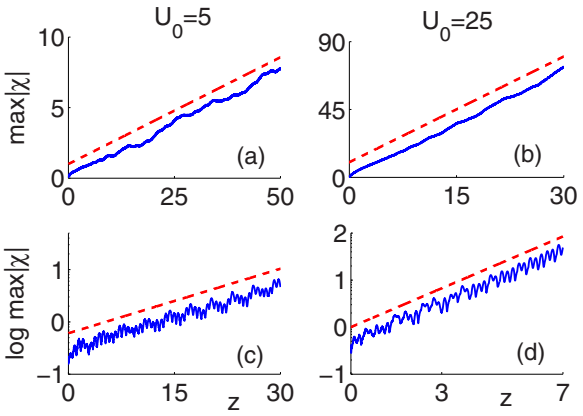

FIG. 21. (Color online) Dynamical evolution of the linear stability problem (25) with initial random perturbation given in Eq. (29) for $\beta = 1/8$. (a, b) correspond to soliton solutions depicted in Figs. 12(f) and 14(f), respectively, for $g = -1$. (c, d) for solutions shown in Figs. 12(c) and 14(c), respectively, with $g = +1$. A linear least-squares fit (dashed line) is also shown with approximate slopes of (a) 0.15, (b) 2.3, (c) 0.041, and (d) 0.28. The logarithm is base 10.

we focus here on moderate potentials (for $g = -1$) with the solution shown in Fig. 12(f) that corresponds to eigenvalue λ deep inside the first gap. As a reminder, this soliton is centered at a lattice minimum. Figure 21(a) shows the dynamics evolution of the quantity $\max_t |\chi(t,z)|$ as a function of z. As is evident, it grows almost at a linear rate (on a linear scale) suggesting an algebraic type of instability (for convenience, a linear least-squares fit is applied to the numerical curve). This can be thought of as a weak instability and its fate for large z would eventually be determined by nonlinear effects that could either enhance or further weaken this instability. We point out that previous works related to linear stability of lattice solitons for the classical NLS equation ($\beta = 0$) [31,47] have found solutions similar in shape to ours to be weakly exponentially unstable [i.e., $0 < \mathrm{Re}(\sigma) \ll 1$]. Those results were obtained using direct discretization methods for Eq. (27) with $\beta = 0$. In essence, the normal higher-order dispersive effects seem not to significantly alter the stability properties of our soliton in comparison to its classical counterpart. To supplement our findings and further study the large z nonlinear dynamics of the soliton we resort to direct numerical simulations. Figure 22 shows the nonlinear evolution of the soliton given in Fig. 12(f) perturbed by a random localized wave in the form of Eq. (29). One immediately notices that this solution maintains a coherent structure for relatively long distances and does not breakup. This further suggests that this algebraic instability is indeed weak and probably is being suppressed by the presence of the nonlinearity. Similar instability trends have been observed as well for the lattice soliton with large potential amplitude shown in Fig. 14(f). It also seems to grow at a polynomial rate [see Fig. 21(b)]. Direct numerical simulation seems to support these findings and indicate, as shown in Fig. 22, that the lattice mode resists the random perturbation and maintains its near original form up to $z = 100$.

Finally, we address the issue of stability related to the gap solitons shown in Figs. 12(c) and 14(c), corresponding to $g = +1$. Notice that both solitons have odd parity and

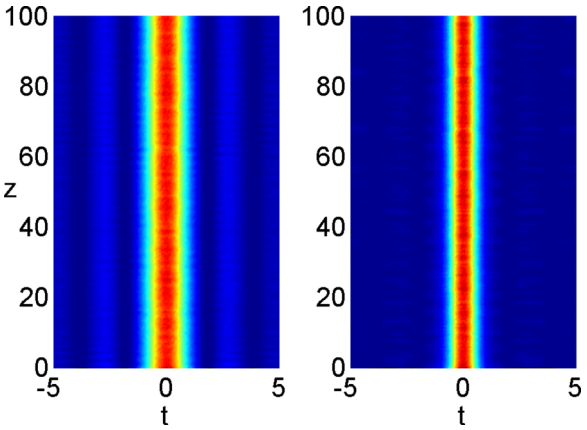

FIG. 22. (Color online) Direct numerical simulation of the lattice soliton shown in Fig. 12(f) with $U_0 = 5$, $\max|\phi| \approx 2.01$ (left) and Fig. 14(f) with $U_0 = 25$, $\max|\phi| \approx 3.94$ (right). For both panels the random perturbation is given by Eq. (29) with $\varepsilon = 0.1$ and $g = -1$.

are centered at a potential minimum with localization length decreasing as a function of U_0. Simulating Eq. (25) with the initial condition given in Eq. (29) reveals that the quantity $\log \max_t |\chi(t,z)|$ measured for both solutions grows linearly in a semilog scale (base 10); see Figs. 21(c) and 21(d). The instability growth rates are readily obtained from a least-squares fit and are approximately given by 0.041 [Fig. 21(c)] and 0.28 [Fig. 21(d)]. The deep lattice soliton is seen to be profoundly more unstable (have a larger growth rate value) compared to its shallow lattice counterpart. To shed more light on the dynamics of the instability we again resort to direct numerical simulations where both solitons are perturbed using the random input (29). Figure 23 reveals a rich internal dynamics for both modes. Most notable is the nonlinear evolution of the soliton residing on the deep lattice where a breakup of the soliton occurs at an early stage of the nonlinear instability. However, this is not the case with the shallow lattice soliton where it seems to disintegrate at a much later distance. This dynamical instability scenario is notably different than the

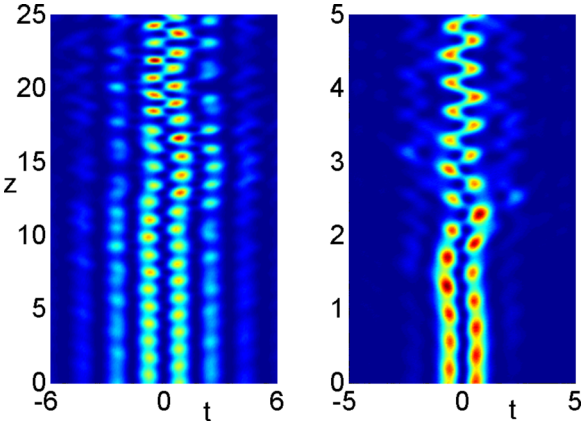

FIG. 23. (Color online) Direct numerical simulation of the lattice soliton shown in Fig. 12(c) with $U_0 = 5$, $\max|\phi| \approx 2.27$ (left) and Fig. 14(c) with $U_0 = 25$, $\max|\phi| \approx 4.32$ (right). For both panels the random perturbation is given by Eq. (29) with $\varepsilon = 0.1$ and $g = +1$.

previous gap lattice soliton one ($g = -1$) where no significant instability was observed. We next point out an interesting link between the stability results shown in Fig. 21 to those in Fig. 23. The growth rate in Fig. 21(d) is roughly seven times larger than that in Fig. 21(c). Notice now that the dramatic onset of instability shown in Fig. 23 for $U_0 = 5$ occurs approximately seven times later ($z \approx 14$) than when $U_0 = 25$ ($z \approx 2$). Due to randomness, each simulation run has a different initial condition with form induced from Eq. (29), yet the linear instability growth rates from Eq. (25) agree quite well with the relative nonlinear instability counterpart. The large z dynamics of both solitons is degeneracy into an alternating pattern of pulses centered at a lattice site. Similar behavior attributed to oscillatory instabilities ($\sigma \in \mathbb{C}$) have been reported in the classical case [31,32]. It was shown in [36,48] that self-focusing first gap solutions display oscillatory instabilities when at least one of the sidebands, $\lambda \pm \mathrm{Im}(\sigma)$, lies inside a spectral band. It should also be noted that given a strong-enough perturbation the solution can jump to other lattice sites, however, we do not show it here.

B. Anomalous dispersion case

Several types of soliton solutions have been identified in Sec. IV B, both in shallow-to-moderate ($U_0 = 10$) as well as the deep lattice ($U_0 = 45$) regimes. Some have their eigenvalues in the semi-infinite gap and others in the first gap (see examples in Figs. 16 and 18). As we have pointed out earlier, since our solution set is relatively large our approach to stability is going to be selective rather than collective. With this in mind, we first present numerical stability results (linear and nonlinear) pertaining to the specific family member shown in Fig. 16(b). We would like to point out that we have also studied the question of stability of other semi-infinite gap soliton solutions with larger potential amplitude like the one shown in Fig. 18(b). Our findings are similar to those presented below. Diagonalizing the eigenvalue problem (27) reveals that the mode shown in Fig. 16(b) is neutrally stable (see Fig. 24).

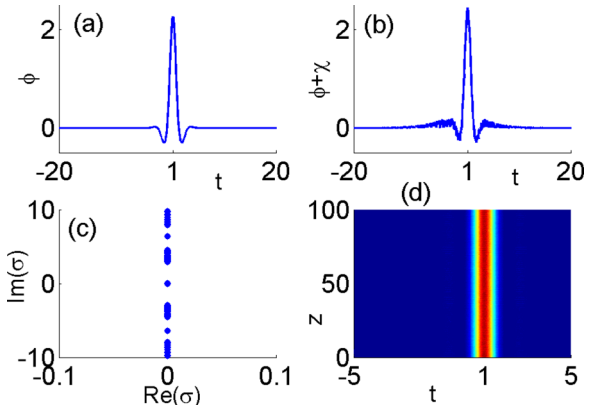

FIG. 24. (Color online) (a) Lattice soliton $\phi(t)$ given in Fig. 16(b) with $\max|\phi| \approx 2.26$. (b) $\phi(t) + \chi(t,0)$ where $\chi(t,0)$ is the perturbation given in Eq. (29) for one realization of randomness and $\varepsilon = 0.1$. (c) Spectrum of the linear stability eigenvalue problem (27) corresponding to the lattice soliton in panel (a). (d) Dynamic stability obtained by direct numerical simulation using Eq. (1) with initial condition shown in panel (b).

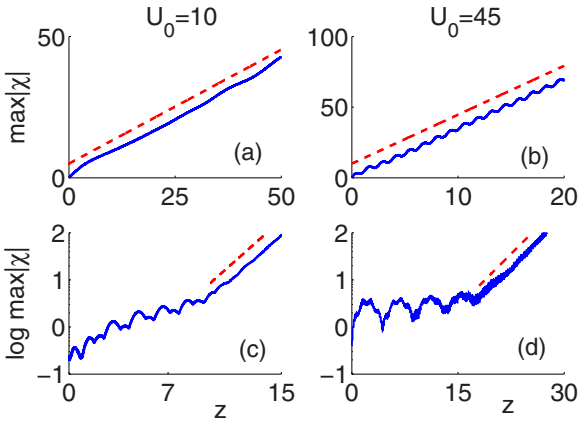

FIG. 25. (Color online) Dynamical evolution of the linear stability problem (25) with initial random perturbation given in Eq. (29) for $\beta = -1/8$. Panels (a, b) correspond to soliton solutions depicted in Figs. 16(e) and 18(e), respectively, for $g = +1$. (c, d) Solutions shown in Figs. 16(d) and 18(d), respectively, with $g = -1$. A linear least-squares fit (dashed line) is also shown with approximate slopes of (a) 0.81, (b) 3.5, (c) 0.27, and (d) 0.15. The logarithm is base 10.

Recall that this solution is centered around a lattice maximum (off-site) at $t = 1$. In [36,48] it was shown that for $\beta = 0$ all off-site soliton solutions are unstable. To confirm our stability findings we perturb the semi-infinite gap solution in Fig. 16(b) with the perturbation of the form (29). Figure 24 shows the dynamical evolution of such a soliton solution, and as one can see, the mode profile remains coherent for long distances.

When discussing the question of linear stability of all first gap solitons, we shall adopt the dynamics approach governed by Eq. (25) subject to initial condition (29) rather than solving the eigenvalue problem (27) that seems to give spurious eigenvalues. In what follows, we shall present results concerning the $g = +1$ high-intensity solutions shown in Figs. 16(e) and 18(e). We reiterate, both solutions are off-site centered at a lattice maximum and exhibit even parity with a slight difference in their so-called fast-scale periodicity. The moderate lattice soliton has a fast-scale periodicity of 4 as opposed to 2 for the deep lattice soliton. This difference is a direct result of the local change in the linear band geometrical structure observed in Sec. II B. A summary of the linear dynamics simulations results is presented in Figs. 25(a) and 25(b). The common feature between the two cases is the development of an algebraic instability. However, the linear least-squares fit indicates that for the deep lattice case the instability grows faster than in the shallow lattice regime. In fact, the direct numerical simulations in Fig. 26 show these solutions, for both moderate and large lattice strengths, do maintain their original shape up to $z = 100$. For the large potential solution, a fine oscillatory structure is present in both Figs. 25(b) and 26.

Finally, the numerical linear and nonlinear stability of the $g = -1$ soliton solutions shown in Figs. 16(d) and 18(d) is analyzed. This time, Fig. 25(c) shows the onset of instability is accompanied by a strong transient dynamic until it relaxes into a well-defined linear growth (in a semilog scale). This is not quite the case observed in Fig. 25(d). Here, the transient motion is "quasiperiodic" that is being washed-out at around

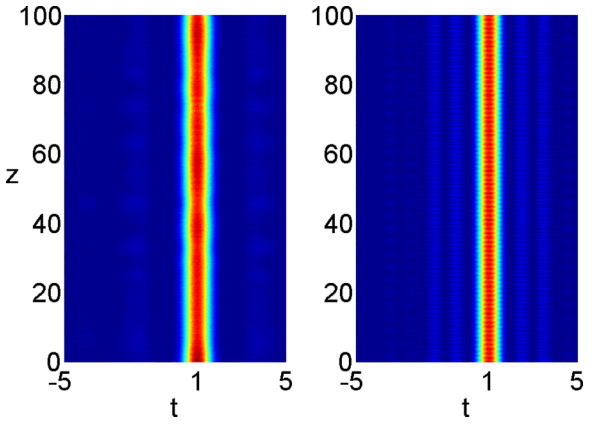

FIG. 26. (Color online) Direct numerical simulation of the lattice soliton shown in Fig. 16(e) with $U_0 = 10$, $\max|\phi| \approx 2.35$ (left) and Fig. 18(e) with $U_0 = 45$, $\max|\phi| \approx 5.11$ (right). For both panels the random perturbation is given by Eq. (29) with $\varepsilon = 0.1$ and $g = +1$.

$z = 20$ after which a linear growth takes over. This scenario is clearly different than the one reported in Figs. 21(c) and 21(d) where no such obvious separation between transient and linear growth periods is seen. A linear least-squares fit is applied to the logarithm base 10 of $\max|\chi|$ as z increases. In Fig. 27, typical evolutions of the instability are shown for these solutions after being perturbed by Eq. (29). In the shallow lattice case, the soliton breaks up into oscillating pulses centered around the lattice maximum $t = 1$. This shifting from on-site to off-site is known as symmetry breaking [36] and has been observed for $\beta = 0$ in excited states. The large potential solution in Fig. 18(d) is off-site and no symmetry-breaking instability occurs, however, it does degenerate into a highly oscillatory set of pulses. We also note the instability appears stronger in Fig. 26(c) at shallower potentials as compared to Fig. 26(d). As the lattice strength increases so does the measure of the band gap and as a result the spectral bands become flatter. Since oscillatory instabilities occur when the sidebands $\lambda \pm \mathrm{Im}(\sigma)$ lie inside FB bands it has been suggested [47] that increasing the lattice strength creates more stable solutions. We

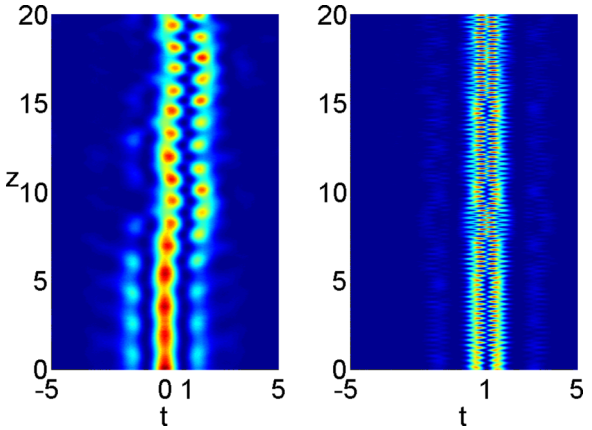

FIG. 27. (Color online) Direct numerical simulation of the lattice soliton shown in Fig. 16(d) with $U_0 = 10$, $\max|\phi| \approx 2.53$ (left) and Fig. 18(d) with $U_0 = 45$, $\max|\phi| \approx 5.31$ (right). For both panels the random perturbation is given by Eq. (29) with $\varepsilon = 0.1$ and $g = -1$.

again remark that strong perturbations can induce solutions to change sites while evolving.

VI. CONCLUSION

In this paper we have extensively studied the dynamical behavior of the biharmonic nonlinear Schrödinger equation in one space dimension and in the presence of an external periodic potential. Various band-gap structures have been numerically computed using the Floquet-Bloch theory. The geometric characteristics of the dispersion curves as a function of the fourth-order dispersion coupling constant β have been identified. In sharp contrast to the classical NLS equation with an external periodic potential for which a gap in the spectrum opens for any nonzero potential, here it is found (for negative β) that there exists a nonzero threshold value of potential strength (dependent on β) below which there is no gap. For increasing values of potential amplitudes, the shape of the dispersion curves changes appreciably giving rise to new families of localized modes that have no counterpart in the classical NLS equation. Part of our numerical results related to the spectral bands are intuitively explained using a higher-order two-band tight-binding model. Lattice solitons corresponding to spectral eigenvalues lying in the the semi-infinite and first band gap were numerically found using a real-space fixed-point renormalization scheme. In the anomalous dispersion case, where for $g = +1$ no localized nonradiating solitons exist in the absence of any external potential, nonlinear finite-energy modes have been identified. Using a combination of linear stability analysis and direct numerical simulations we have addressed the question of stability for various localized lattice modes.

ACKNOWLEDGMENT

The work of J.T.C. and Z.H.M was supported in part by NSF Grant No. DMS-0908599.

APPENDIX A: COMPUTATION OF BAND STRUCTURE

In this section we briefly outline the numerical scheme used to construct the FB band structures. The method is based on expanding the eigenfunction and potential in Floquet-Fourier series (also known as *Hill's Method* [49])

$$F(t,\mu) = \sum_{n\in\mathbb{Z}} C_n(\mu) e^{i(\omega_n+\mu)t}\,, \tag{A1}$$

$$V(t) = \sum_{m\in\mathbb{Z}} V_m e^{i\omega_m t}\,, \tag{A2}$$

for $\omega = 2\pi/T$ and $\omega_n = n\omega$. Substituting Eqs. (A1) and (A2) into Eq. (2) gives an infinite-dimensional algebraic system for the Fourier coefficients $C_j, j \in \mathbb{Z}$

$$\Omega(\mu+\omega_j)C_j(\mu) + \sum_{\ell\in\mathbb{Z}} V_\ell C_{j-\ell}(\mu) = \lambda(\mu)C_j(\mu)\,, \tag{A3}$$

with $\Omega(\xi) \equiv \xi^2/2 + \beta\xi^4$. For μ in the first BZ $[-\pi/T, \pi/T]$ we truncate system (A3) on the lattice sites to $j = -N/2, \ldots, N/2$ (for even N) and obtain the following

eigenvalue problem

$$\mathbb{P}(\mu)\mathbf{C} = \lambda\mathbf{C}\ , \tag{A4}$$

where

$$\mathbb{P}(\mu)=\begin{pmatrix} \Omega_{-\frac{N}{2}} & V_1^* & & & \\ V_1 & \Omega_{-\frac{N}{2}+1} & \ddots & & \\ & \ddots & \ddots & & \\ & & & \Omega_{\frac{N}{2}-1} & V_1^* \\ & & & V_1 & \Omega_{\frac{N}{2}} \end{pmatrix}, \tag{A5}$$

and $\mathbf{C} = (C_{-N/2},\ldots,C_{N/2})^T$; $\Omega_j \equiv V_0 + \Omega(\mu+\omega_j)$. For potential (8) the Fourier coefficients are $V_0 = U_0/2$ and $V_1 = -U_0/4 = V_1^*$. An alternate method of finding the band structure is to represent the derivatives in Eq. (2) by differentiation matrices and collocate the potential function at the nodal values. To do so, we substitute Eq. (5) into Eq. (2); expand the resulting operator $\mathbb{W}_\beta(\partial_t + i\mu)$ in powers of μ; then represent each derivative by its corresponding differentiation matrices giving the computational problem

$$\begin{aligned} &\left[\beta D^{(4)} - \tfrac{1}{2}D^{(2)} + \mathrm{diag}(V_j)\right]G = \lambda G\ , \\ &D^{(4)} = \mathbb{D}_4 + 4i\mu\mathbb{D}_3 - 6\mu^2\mathbb{D}_2 - 4i\mu^3\mathbb{D}_1 + \mu^4\ , \\ &D^{(2)} = \mathbb{D}_2 + 2i\mu\mathbb{D}_1 - \mu^2\ , \end{aligned} \tag{A6}$$

where $V_j = V(t_j)$ and $\mathbb{D}_n$ represents either the finite difference or spectral periodic differentiation matrices of the nth derivative. Only μ in the first BZ need to be considered due to periodicity.

APPENDIX B: FIXED-POINT RENORMALIZATION METHOD

Here, we present the real-space fixed-point renormalization scheme [50] used in this paper to numerically compute lattice solitons. Substituting the waveguide solutions of the form $E(t,z) = \phi(t)e^{-i\lambda z}$ into Eq. (1) gives

$$(\mathbb{W}_\beta - \lambda)\phi = g|\phi|^2\phi\ , \tag{B1}$$

for $\mathbb{W}_\beta(\partial_t) \equiv \beta\partial_t^4 - \partial_t^2/2 + V(t)$. Now set $\phi = r\Psi$, for constant r, substitute into Eq. (B1); and take the inner product of the resulting equation with Ψ yielding

$$|r|^2 = \frac{\langle\Psi, \mathbb{W}_\beta\Psi\rangle - \lambda||\Psi||_2^2}{g||\Psi||_4^4}\ , \tag{B2}$$

where

$$\begin{aligned} ||f||_p^p &:= \int_{\mathbb{R}} |f|^p dt\ , \\ \langle h_1, h_2\rangle &= \int_{\mathbb{R}} h_1^*(t)h_2(t)dt\ . \end{aligned}$$

This rescaled solution is approximated by the equation

$$\mathcal{L}\Psi = g|r|^2|\Psi|^2\Psi\ , \quad \mathcal{L} = \beta\mathbb{D}_4 - \tfrac{1}{2}\mathbb{D}_2 + \mathrm{diag}(V_j - \lambda)\ , \tag{B3}$$

where $\mathbb{D}_2$ and $\mathbb{D}_4$ are the spectral or finite-difference differentiation matrices corresponding to ∂_t^2 and ∂_t^4, respectively, and $V_j = V(t_j)$. Note that for λ residing in the band gaps, the matrix on the left-hand side of Eq. (B3) is invertible. We further rewrite Eq. (B3) as follows

$$\Psi = \mathcal{Q}(\Psi)\ , \tag{B4}$$

for $\mathcal{Q}(\Psi) = g|r|^2\mathcal{L}^{-1}(|\Psi|^2\Psi)$. In some cases, for example, with highly nonlinear lattice modes, the direct successive approximation applied to Eq. (B4) fails to converge. To overcome this difficulty, we employ the successive overrelaxation fixed-point renormalization scheme where we multiply Eq. (B4) by a fixed positive relaxation factor α and then add Ψ to both sides. This suggests the iterative method

$$\Psi_{n+1} = (1-\alpha)\Psi_n + \alpha\mathcal{Q}(\Psi_n)\ ; \tag{B5}$$

when $\alpha = 1$, Eq. (B5) reduces to the spectral renormalization method.

[1] G. P. Agarawal, *Nonlinear Fiber Optics* (Academic, New York, 2012).

[2] Y. S. Kivshar and G. P. Agarawal, *Nonlinear Fiber Optics* (Academic, New York, 2003).

[3] D. N. Christodoulides, F. Lederer, and Y. Silberberg, Nature (London) **424**, 817 (2003).

[4] D. N. Christodoulides and R. J. Joseph, Opt. Lett. **13**, 794 (1988).

[5] N. K. Efremidis, S. Sears, D. N. Christodoulides, J. W. Fleischer, and M. Segev, Phys. Rev. E **66**, 046602 (2002).

[6] J. W. Fleischer, T. Carmon, M. Segev, N. K. Efremidis, and D. N. Christodoulides, Phys. Rev. Lett. **90**, 023902 (2003).

[7] J. Fleischer, M. Segev, N. Efremidis, and D. N. Christodoulides, Nature (London) **422**, 147 (2003).

[8] M. J. Ablowitz, B. Ilan, E. Schonbrun, and R. Piestun, Theo. Math. Phys. **151**, 723 (2007).

[9] Z. H. Musslimani and J. Yang, J. Opt. Soc. Am. B **21**, 973 (2004).

[10] P. G. Kevrekidis, K. O. Rasmussen, and A. R. Bishop, Int. J. Mod. Phys. B **15**, 2833 (2001).

[11] Y. V. Karashov, B. A. Malomed, and L. Torner, Rev. Mod. Phys. **83**, 247 (2011).

[12] K. G. Makris, J. Hudock, D. N. Christodoulides, G. I. Stegeman, O. Manela, and M. Segev, Opt. Lett. **31**, 2774 (2006).

[13] Z. H. Musslimani, K. G. Makris, R. El-Ganainy, and D. N. Christodoulides, Phys. Rev. Lett. **100**, 030402 (2008).

[14] K. G. Makris, R. El-Ganainy, D. N. Christodoulides, and Z. H. Musslimani, Phys. Rev. Lett. **100**, 103904 (2008).

[15] C. E. Rüter, K. G. Makris, R. El-Ganainy, D. N. Christodoulides, M. Segev, and D. Kip, Nat. Phys. **6**, 192 (2010).

[16] A. Guo, G. J. Salamo, D. Duchesne, R. Morandotti, M. Volatier-Ravat, V. Aimez, G. A. Siviloglou, and D. N. Christodoulides, Phys. Rev. Lett. **103**, 093902 (2009).

[17] I. V. Barashenkov, D. E. Pelinovsky, and E. V. Zemlyanaya, Phys. Rev. Lett. **80**, 5117 (1998).

[18] J. Yang, I. Makasyuk, P. G. Kevrekidis, H. Martin, B. A. Malomed, D. J. Frantzeskakis, and Z. Chen, Phys. Rev. Lett. **94**, 113902 (2005).
[19] P. G. Kevrekidis, D. J. Frantzeskakis, R. Carretero-Gonzalez, B. A. Malomed, G. Herring, and A. R. Bishop, Phys. Rev. A **71**, 023614 (2005).
[20] M. A. Porter, R. Carretero-Gonzalez, P. G. Kevrekidis, and B. A. Malomed, Chaos **15**, 015115 (2005).
[21] D. E. Pelinovksy, *Localization in Periodic Potentials* (Cambridge University Press, Cambridge, England, 2011).
[22] M. Skorobogatiy and J. Yang, *Photonic Crystal Guiding* (Cambridge University Press, Cambridge, England, 2011).
[23] C. Denz, S. Flach, and Y. S. Kivshar, *Nonlinearities in Periodic Structures and Metamaterials* (Springer, New York, 2010).
[24] A. Fratalocchi, G. Assanto, K. A. Brzdakiewicz, and M. A. Karpierz, Opt. Lett. **29**, 1530 (2004).
[25] A. Fratalocchi and G. Assanto, Opt. Express **14**, 2021 (2006).
[26] A. Fratalocchi, G. Assanto, K. A. Brzdakiewicz, and M. A. Karpierz, Opt. Express **13**, 1808 (2005).
[27] A. Fratalocchi and G. Assanto, Appl. Phys. Lett. **86**, 051109 (2005).
[28] A. Fratalocchi, G. Assanto, K. A. Brzdakiewicz, and M. A. Karpierz, Opt. Lett. **30**, 174 (2005).
[29] L. N. Trefethen, *Spectral Methods in* MATLAB (SIAM, Philadelphia, 2000).
[30] J. A. C. Weideman and S. C. Reddy, ACM Trans. Math. Soft. **26**, 465 (2000).
[31] P. J. Y. Louis, E. A. Ostrovskaya, C. M. Savage, and Y. S. Kivshar, Phys. Rev. A **67**, 013602 (2003).
[32] N. K. Efremidis and D. N. Christodoulides, Phys. Rev. A **67**, 063608 (2003).
[33] N. K. Efremidis and D. N. Christodoulides, Phys. Rev. E **65**, 056607 (2002).
[34] V. I. Karpman, Phys. Lett. A **160**, 531 (1991).
[35] G. Fibich, B. Ilan, and G. Papanicolaou, SIAM J. Appl. Math. **62**, 1437 (2002).
[36] D. E. Pelinovsky, A. A. Sukhorukov, and Y. S. Kivshar, Phys. Rev. E **70**, 036618 (2004).
[37] J. Yang, *Nonlinear Waves in Integrable and Nonintegrable Systems* (SIAM, Philadelphia, 2010).
[38] I. V. Barashenkov and E. V. Zemlyanaya, Comput. Phys. Comm. **126**, 22 (2000).
[39] J. Schöllmann, Phys. A **288**, 218 (2000).
[40] J. Yang, J. Comput. Phys. **227**, 6862 (2008).
[41] E. Blank and T. Dohnal, SIAM J. Appl. Dyn. Sys. **10**, 667 (2011).
[42] T. Kapitula and B. Standstede, Physica D **124**, 58 (1998).
[43] T. Kapitula, SIAM J. Math. Anal. **30**, 273 (1999).
[44] G. Hwang, T. R. Akylas, and J. Yang, Stud. Appl. Math. **128**, 275 (2012).
[45] Y. Sivan, G. Fibich, B. Ilan, and M. I. Weinstein, Phys. Rev. E **78**, 046602 (2008).
[46] B. Ilan, Y. Sivan, and G. Fibich, Opt. Lett. **36**, 397 (2011).
[47] T. Richter, K. Motzek, and F. Kaiser, Phys. Rev. E **75**, 016601 (2007).
[48] A. A. Sukhorukov and Y. S. Kivshar, Opt. Lett. **28**, 2345 (2003).
[49] B. Deconinck and J. N. Kutz, J. Comp. Phys. **219**, 296 (2006).
[50] M. J. Ablowitz and Z. H. Musslimani, Opt. Lett. **30**, 2140 (2005).